

Imaging the Solar Tachocline by Time-Distance Helioseismology

Junwei Zhao¹, Thomas Hartlep^{2*}, A. G. Kosovichev¹, and N. N. Mansour²

ABSTRACT

The solar tachocline at the bottom of the convection zone is an important region for the dynamics of the Sun and the solar dynamo. In this region, the sound speed inferred by global helioseismology exhibits a bump of approximately 0.4% relative to the standard solar model. Global helioseismology does not provide any information on possible latitudinal variations or asymmetries between the northern and southern hemisphere. Here, we develop a time-distance helioseismology technique, including surface- and deep-focusing measurement schemes and a combination of both, for two-dimensional tomographic imaging of the solar tachocline that infers radial and latitudinal variations in the sound speed. We test the technique using artificial solar oscillation data obtained from numerical simulations. The technique successfully recovers the major features of simplified tachocline models. The technique is then applied to SOHO/MDI medium- ℓ data and provides for the first time a full two-dimensional sound-speed perturbation image of the solar tachocline. The one-dimensional radial profile obtained by latitudinal averaging of the image is in good agreement with the previous global helioseismology result. It is found that the amplitude of the sound-speed perturbation at the tachocline varies with latitude, but it is not clear whether this is in part or fully an effect of instrumental distortion. Our initial results demonstrate that time-distance helioseismology can be used to probe the deep interior structure of the Sun, including the solar tachocline.

Subject headings: Sun: helioseismology — Sun: Activity — Sun: Interior — Sun: Magnetic Fields

1. Introduction

The solar tachocline, first defined by Spiegel & Zahn (1992), is a region located between the solar convection zone and the radiative zone. It is a transition zone where the latitudinal differential

¹W.W.Hansen Experimental Physics Laboratory, Stanford University, Stanford, CA 94305-4085

²NASA Ames Research Center, Mailstop 230-2, Moffet Field, CA 94035

*present address: W.W.Hansen Experimental Physics Laboratory, Stanford University, Stanford, CA 94305-4085

rotation of the convection zone changes to a rigid rotation of the radiative zone, as found by numerous helioseismology studies (e.g., Thompson et al. 1996; Schou et al. 1998). In this region the inferred sound-speed perturbation profile exhibits the largest difference relative to a standard solar model - Model S (Christensen-Dalsgaard et al. 1996), as revealed by a number of helioseismology studies (e.g., Gough et al. 1996; Kosovichev et al. 1997). The solar tachocline is also widely believed to be the location where the solar dynamo operates, since the sharp rotational gradient observed in this area can build up a strong toroidal field (e.g., Parker 1993; Charbonneau & MacGregor 1997; Dikpati & Charbonneau 1999). Therefore, it is important to measure the structure, dynamics, and cyclic variations of the tachocline. Measurements in this zone will provide a better understanding of the transition from the solar convection zone to the radiative zone, the mechanisms of solar magnetic field generation and amplification, as well as the periodicity and evolution of the solar activity cycles.

However, despite the importance of the tachocline, little is known about this area from observations besides the steep rotational shear and the one-dimensional sound-speed perturbation bump. This region is difficult to probe by helioseismology because it is quite thin, $\sim 0.05 - 0.09R_{\odot}$ (Kosovichev 1996b; Basu 1997), and is located deep in the Sun, approximately $0.29R_{\odot}$ below the photosphere (Christensen-Dalsgaard et al. 1991). Nearly all observational results related to the tachocline area were obtained by global helioseismology analysis of normal mode frequencies, which is not capable of resolving hemispheric asymmetries of the differential rotation and sound-speed structures. In this paper, we explore the possibility of mapping a two-dimensional image of the tachocline, both latitude and depth dependent, by the use of time-distance helioseismology (Duvall et al. 1993), a local helioseismology technique.

Because helioseismology infers solar interior properties that are undetectable by other independent observations, it is often difficult to assess the quality and accuracy of the inferred properties. Recently, Georgobiani et al. (2007) and Zhao et al. (2007) evaluated the performance of the time-distance technique for inferring small-scale subsurface flow fields by analyzing data from numerically simulated solar convection (Bensen et al. 2006), and found satisfactory results. More recently, Hartlep et al. (2008) validated the time-distance far-side imaging technique (Zhao 2007) by using numerical simulations of the global acoustic wavefields of the whole Sun. In this paper, we use a similar approach: develop time-distance measurement and inversion procedures for imaging sound-speed variations in the tachocline, test these procedures on numerical simulation data, and finally apply the procedures to actual observations.

To image the solar tachocline, we develop two time-distance measurement procedures based on surface- and deep-focusing schemes (Duvall 2003), and the corresponding inversion codes, and also use a code to invert combined measurements of these two schemes. A description of the measurement and inversion techniques is given in Sec. 2. In Sec. 3 we describe the application of

our method to numerical simulation data, and assess the performance of our method. In Sec. 4, we present initial results of the tomographic imaging of the solar tachocline using *SOHO*/MDI data (Scherrer et al. 1995). A brief discussion follows in Sec. 5.

2. Techniques

2.1. Surface- and Deep-Focusing Measurements

Time-distance helioseismology measures travel times of acoustic waves that propagate from one solar surface location to another along curved paths through the solar interior. These measurements are done by computing the cross-correlation between acoustic signals observed at these two separate locations. In practice, in order to improve the signal to noise ratio, the cross-correlations are calculated between the acoustic signal observed at a given point and the signal averaged over its surrounding annulus or part of the annulus. When all ray paths converge at one surface location in such measurements, as shown in Fig. 1a, this measurement scheme is often called surface-focusing. When all ray paths pass through one point located in the solar interior, this scheme is often referred to as deep-focusing (Fig. 1b).

The measurement procedure is as follows: A datacube of a time sequence of surface velocity images, either numerically simulated or observed, is remapped into heliographic coordinates (using Postel’s projection) with the center of the projected map located at the solar disk center and a pixel size of 0.6° (hereafter, degree means heliographic degree), consistent with the MDI medium- ℓ data sampling resolution. For the surface-focusing scheme every pixel in the dataset serves as a central point, and for each central point the acoustic signals are averaged over a set of annuli around this point. Each annulus corresponds to a particular range of travel distances of acoustic waves. The radius of the annuli ranges from 6.0° to 84.0° with a step of 0.6° , hence a total of 131 annuli (travel distances) are used. This number is significantly greater than the number of annuli used in most previous time-distance helioseismology measurements. At each location, the cross-correlations are computed between the signals at the central point and the signals from each annulus. To further improve the signal-to-noise ratio, we average the cross-correlations in overlapping latitudinal zones 5.0° wide, from -60° to 60° with a step of 0.6° . Then, we use the Gabor wavelet fitting procedure (Kosovichev & Duvall 1997) to derive the mean acoustic phase travel times for all annuli at each latitude.

For the deep-focusing scheme (Fig. 1b), every pixel also serves as a central point, but the annuli are divided into four quadrants in the North, East, South, and West directions. The acoustic signals are averaged in each quadrant, and cross-correlations are calculated between opposite quadrants. Then, these two cross-correlations are averaged together. Note that for some locations,

not both cross-correlations can be obtained, since some quadrant annuli may be located beyond the solar limbs or poles. In these measurements, the distance between the opposite quadrants varies from $6^\circ 0$ to $84^\circ 0$ with a step of $1^\circ 2$; hence, a total of 66 travel distances is used. Similar to the surface-focusing scheme, the cross-correlations are averaged in longitudinal belts, and the Gabor wavelet fitting is performed to derive the acoustic travel time for each annulus and each latitudinal belt.

It is important to note that unlike in most other time-distance helioseismology studies no phase-speed filtering is used in the travel time calculations in this study, because for the large distances used in this study, such filtering may introduce systematic shifts that are not fully understood (Duvall 2003). However, as usual, solar convection and f -modes are removed by filtering.

2.2. Inversion Algorithm

After the acoustic travel times are measured an inversion procedure is applied to infer the sound-speed perturbations inside the Sun. The travel-time sensitivity kernels in spherical coordinates are calculated using the ray-path approximation (D’Silva & Duvall 1995). The sensitivity kernels are computed separately for the two different measurement schemes. First, three-dimensional kernels are computed for all different annuli, and the kernels are then averaged along the longitudinal direction to make the kernels depend only on latitude and radius.

The inversions are performed by solving the linearized equations for the travel time variations in the sense of least squares (Kosovichev & Duvall 1997). Generally, two different inversion algorithms were used in the past in time-distance helioseismology, LSQR algorithm (Kosovichev 1996a; Zhao, Kosovichev, & Duvall 2001) and Multi-Channel Deconvolution, also known as MCD (e.g., Jacobsen et al. 1999; Couvidat et al. 2005). In this paper, we employ the MCD technique. Although the inversions in this study would be performed in spherical coordinates, MCD is still usable when the interior vertical grids are divided along the radial direction, and when the boundaries are properly taken into account.

3. Results from Numerical Simulation Data

3.1. Model and Numerical Simulation

A numerical simulation code has been developed to simulate the three-dimensional acoustic wavefields of the global Sun in spherical coordinates (Hartlep & Mansour 2008). It solves the linearized Euler equations describing wave propagation excited by random sources near the surface.

In the present study, the simulations include oscillations of spherical degree, ℓ , in the range from 0 to 170. This is sufficient for most global scale studies. Comparing with observations obtained from the MDI medium- ℓ program, this simulation code reproduces accurately the solar oscillation power spectrum ($k - \omega$ diagram) except at high frequencies. It also reproduces the acoustic travel times measured by the time-distance technique (see Fig. 1 in Hartlep et al. 2008). Global wavefields generated with this simulation code have been successfully used for validating the time-distance far-side imaging technique (Hartlep et al. 2008).

The sound-speed perturbation near the solar tachocline observed by global helioseismology is measured relative to a standard solar model, Model S (Christensen-Dalsgaard et al. 1996). Therefore, to infer the sound-speed structure at the tachocline from the measured acoustic travel times, it is necessary to subtract the corresponding reference travel times measured from a simulation for the unperturbed Model S. A latitudinally averaged reference time-distance curve obtained for the surface-focusing scheme is shown in Fig. 2. The time-distance relationship for the deep-focusing scheme is similar.

For testing, we use an artificial model of the sound-speed perturbations in the tachocline shown in Fig. 3. The perturbed structure has a two-dimensional Gaussian shape in each hemisphere, but is asymmetric relative to the equator. The maximum amplitudes of sound-speed perturbation, 0.7% in the Northern hemisphere and 0.5% in the Southern hemisphere, are not far apart from the values derived from global helioseismology (e.g., Kosovichev et al. 1997). The perturbation in each hemisphere is centered at $0.70R_{\odot}$ with a FWHM of $0.082R_{\odot}$ (the variance of the Gaussian is $0.035R_{\odot}$) in the radial direction, and centered at latitude of 30° with a FWHM of 35° (variance of 15°). The time series from the numerical simulations of the acoustic wavefields for both unperturbed and perturbed models are 1024 minutes long.

3.2. Surface-Focusing Results

For the surface-focusing scheme the measured acoustic travel times after subtraction of the reference travel times are shown in Fig. 4a as a function of the annulus radius (travel distance) and latitude. One can easily see that the travel times are apparently smaller on the right-hand side of the image when the radius is larger than 46° . This can be better identified in the 1D curves obtained after latitudinal averaging in both hemispheres, as shown in Fig. 4b.

The inversion results for the surface-focusing scheme (Fig. 4c,d) show that the model sound-speed perturbation in the tachocline area is recovered, although it does not perfectly match the two Gaussian shaped structures in both hemispheres. The location and amplitude of the perturbation match well. However, it is obvious from the sound-speed image (Fig. 4c) and the latitudinally

averaged 1D sound-speed perturbation curves from both hemispheres (Fig. 4d), that the inverted sound-speed perturbation is wider than the prescribed model, especially into the deeper interior. A negative sidelobe close to the surface can also be seen.

It is not immediately clear why the inverted sound-speed results are not well localized in the deeper area. Inversion averaging kernels, which characterize the spatial resolution, are displayed in Fig. 5 for three different targeted depths inside the Sun. It can be seen that when the target is located near the bottom of the convection zone the averaging kernel is more spread in latitude, and that the kernel is more spread in the radial direction when the target location is shallower. Nevertheless, the averaging kernels are well localized and should not be the reason for the spreading of the inverted sound-speed perturbation. We suspect that the poor localization with depth below the tachocline is caused by the use of ray-path sensitivity kernels and by relatively high realization noise in the simulation data, which is significantly higher than in the real data since the simulation time series are shorter. The inversion may be improved by the use of Born-approximation kernels (e.g., Birch & Kosovichev 2000), longer time series, and more realistic wave excitation models.

3.3. Deep-Focusing Results

The measurement and inversion results for the deep-focusing scheme are presented in Fig. 6. Similar to the surface-focusing measurements, a travel-time drop can be easily identified at an annulus radius of $\sim 45^\circ$ from both the 2D travel-time image (Fig. 6a) and the 1D latitudinally averaged curves (Fig. 6b). It is noteworthy that at high latitudes and large annulus radii, the acoustic travel-time measurements are often unreliable because there are too few pixels available for averaging. The measurements in these areas are discarded to make sure that the inversion results are not contaminated by bad fitting points.

The inversion results for the deep-focusing scheme are shown in Fig. 6c,d. Similar to the surface-focusing inversion results, the sound-speed bump is successfully recovered, although the shape does not perfectly match the model. Again, the inferred sound-speed perturbation is spread into areas below the tachocline region. Despite that the averaging kernels for the deep-focusing inversions (Fig. 7) are well localized, even better than for the surface-focusing inversions, the noise level of the inverted results is higher. Of course, there is a trade-off between localization and noise amplification in the inversion results. In the model calculations, the trade-off parameter is chosen to get good localization in the tachocline region. We did not try to optimize the inversion procedure for the deeper interior. The same regularization parameters are used for inversion of the real data.

3.4. Results from a Combination of Surface- and Deep-Focusing

The surface- and deep-focusing measurement schemes use the same datasets but are different analysis procedures, and have different sensitivities and signal-to-noise ratios at different depths. Thus, it is useful to combine the acoustic travel time measurements from both schemes, and make one inversion to improve the results. It is expected that such joint inversion would improve localization of the inversion results and enhance the signal-to-noise ratio. It is not difficult to revise the inversion code to solve two sets of linear integral equations instead of one using a proper combination of the surface- and deep-focusing sensitivity kernels and measured travel times.

The inversion results are shown in Fig. 8. As it can be seen, both the 2D and 1D results look similar to an average of the separate inversion results of the surface- and deep-focusing schemes. Generally, the inversion from the combined measurements is closer to the model than each separate inversion. The averaging kernels from this inversion also look similar to the average of the averaging kernels of these measurement schemes, and are not shown here.

4. Results from SOHO/MDI Observations

4.1. Data Processing

The medium- ℓ program of the MDI instrument onboard *SOHO* (Kosovichev et al. 1997) provides nearly continuous space observations of solar oscillation modes with angular degree ℓ ranging from 0 to ~ 300 . The medium- ℓ data represent Doppler velocity images acquired with 1-minute cadence and a spatial sampling of $10''$ (0.6 heliographic degrees per pixel) after some averaging onboard the spacecraft and ground calibration. These data can be used for imaging the solar tachocline and studying its evolution with the solar cycle.

We select the MDI observations from July 25 through August 22, 1996, covering the whole Carrington rotation CR1912. This period is during the solar minimum between solar cycles 22 and 23. This helps to avoid potential complications caused by strong surface magnetic fields present during other periods of the solar cycle. For each day of the observations (1440 minutes long), we remap the data into heliospheric Carrington coordinates using Postel’s projection. The main purpose of this remapping is to filter out the signals of solar convection and f -mode oscillations. For each observation day, we calculate and save the cross-correlation functions for both the surface- and deep-focusing measurements. Then, the daily cross-correlations are averaged for the whole Carrington rotation, and Gabor wavelet fitting is performed. This procedure improves the signal-to-noise ratio. The travel-time inversions are done for this Carrington rotation for the surface- and deep-focusing schemes separately, and their combination, after the corresponding reference travel

times computed from the unperturbed simulation (shown in Fig. 2) are subtracted.

4.2. Measurement and Inversion Results

The measured acoustic travel times and inversion results from the surface-focusing scheme, averaged over the whole Carrington rotation, are presented in Fig. 9. The 2D travel time image has many thin vertical stripes because of noise in the reference travel times calculated from the simulated Sun data. A significant travel time dip can be easily identified at the annulus radius between $\sim 45^\circ$ and $\sim 60^\circ$, corresponding to the sound-speed perturbation bump near the tachocline region (Fig. 9b). The 2D image of the sound-speed perturbations obtained by inversion (Fig. 9c) clearly shows a bump at the location of approximately $0.67R_\odot$. We find that the perturbation at the base of the convection zone is not latitudinally uniform, being weaker near low latitudes and stronger in latitudes higher than about 20° .

The results for the deep-focusing scheme are presented in Fig. 10. The noise level is significantly larger for this scheme than for the surface-focusing scheme. Therefore, we applied a 3-pixel boxcar average to the 2D travel-time image (Fig. 10a), and used the averaged data for inversion. Similar to the surface-focusing results, the acoustic travel times reveal a significant dip for annulus radii from about 46° to 70° . Besides this dark vertical stripe, one can also identify in Fig. 10a white and dark curved band features in both hemispheres, extending from an annulus radius of 6° to nearly 40° and between 30° and 60° in latitude. It is not clear to us whether these features are artifacts or caused by sound-speed perturbations in the Sun. The inversion sound-speed results (Fig. 10c-d) are quite similar to the surface-focusing scheme inferences. The sound-speed bump can be clearly identified, and the perturbation exhibits an apparent latitudinal dependence as well.

The inversion results from a combination of both surface- and deep-focusing measurements are shown in Fig. 11. Because the surface-focusing measurements have a better signal-to-noise ratio and cover higher latitudes than the deep-focusing scheme, we intentionally give a higher weighting to the surface-focusing measurements in these inversions. The selection of this weighting parameter is quite arbitrary, and the weighting has been chosen as 60% for the surface-focusing and 40% for the deep-focusing measurement. It seems that such combined measurements are useful, but may still need further optimization.

It is important to compare our sound-speed profiles with the results from global helioseismology obtained by inversion of normal mode frequencies. Figure 12 shows the comparison of the global helioseismology result obtained from the same SOHO/MDI medium- ℓ data (Kosovichev et al. 1997) with the sound-speed perturbation inferred from the combined measurements in this study. It is found that both results are in good agreement in terms of location and magnitude of the

sound-speed bump near the tachocline, as well as in the convection zone.

The good agreement of the latitudinally averaged sound-speed perturbation with the previous global helioseismology result indicates that our measurements are generally correct. However, the latitudinal variation of the perturbation is surprising. It certainly requires further investigation, in particular, of MDI instrumental distortion (Korzennik et al. 2004) and non-uniform MTF effects.

5. Discussion

Using numerically simulated global acoustic wavefields and solar oscillation observations from SOHO/MDI, we have demonstrated for the first time that time-distance helioseismology is capable of measuring sound-speed perturbations in the tachocline located about 200 Mm beneath the solar photosphere that are relatively small in magnitude and size. This local helioseismology method provides 2D images of these perturbations as a function of latitude and depth. This newly developed technique has an advantage over global helioseismology in that it can distinguish sound-speed perturbations of different amplitude located at different latitude, and is not limited to the North-South symmetrical part. Although we only present in this paper an example with maximum perturbations of 0.7% and 0.5%, our experiments demonstrate that the technique is capable of measuring the North-South difference in the sound-speed structure of the tachocline as small as 0.05%.

Our inversions of the numerical simulation data have shown that although we can recover the major features in the tachocline region, the inferred sound-speed perturbations are more widely spread into areas beneath the tachocline. We think this may be caused by the ray-approximation sensitivity kernels used in our inversions or by the relatively high realization noise in the simulated wavefield. We plan to continue the work on improving the resolution of the deep interior beneath the tachocline.

Our initial analysis of the MDI data shows a latitudinal dependence of sound-speed perturbation at the tachocline. We believe this needs further investigation and modeling of potential instrumental effects. Furthermore, it will be extremely useful to investigate how the tachocline varies with the solar cycle, and we plan to continue these studies in this direction.

REFERENCES

Basu, S. 1997, *MNRAS*, 288, 572

Birch, A. C., & Kosovichev, A. G. 2000, *Sol. Phys.*, 192, 193

- Bensen, D., Stein, R., & Nordlund, Å. 2006, in ASP Conf. Ser. 354, *Solar MHD Theory and Observations: A High Spatial Resolution Perspective*, ed. H. Uitenbroek, J. Leibacher, & R. F. Stein (San Francisco: ASP), 92
- Charbonneau, P., & MacGregor, K. B. 1997, *ApJ*, 486, 502
- Christensen-Dalsgaard, J., Gough, D. O., & Thompson, M. J. 1991, *ApJ*, 378, 413
- Christensen-Dalsgaard, J., et al. 1996, *Science*, 272, 1286
- Couvidat, S., Gizon, L., Birch, A. C., Larsen, R. M., & Kosovichev, A. G. 2005, *ApJS*, 158, 217
- Dikpati, M., & Charbonneau, P. 1999, *ApJ*, 518, 508
- D’Silva, S., & Duvall, T. L., Jr. 1995, *ApJ*, 438, 454
- Duvall, T. L., Jr. 2003, in *Proc. of SOHO 12/ GONG+ 2002 Workshop: Local and Global Helioseismology, the Present and Future (ESA SP-517)*, 259
- Duvall, T. L., Jr., Jefferies, S. M., Harvey, J. W., & Pomerantz, M. A. 1993, *Nature*, 362, 430
- Georgobiani, D., Zhao, J., Kosovichev, A. G., Bensen, D., Stein, R. F., & Nordlund, Å. 2007, *ApJ*, 657, 1157
- Gough, D. O., et al. 1996, *Science*, 272, 1296
- Hartlep, T., & Mansour, N. N. 2008, arXiv:0805.0571
- Hartlep, T., Zhao, J., Kosovichev, A. G., & Mansour, N. N. 2008, *ApJ*, 689, 1373
- Jacobsen, B. H., Møller, I., Jensen, J. M., & Effersø, F. 1999, *Phys. Chem. of the Earth A - Solid Earth and Geodesy*, 24, 15
- Korzennik, S. G., Rabello-Soares, M. C., & Schou, J. 2004, *ApJ*, 602, 481
- Kosovichev, A. G. 1996a, *ApJ*, 461, L55
- Kosovichev, A. G. 1996b, *ApJ*, 469, L61
- Kosovichev, A. G., et al. 1997, *Sol. Phys.*, 170, 43
- Kosovichev, A. G., & Duvall, T. L., Jr. 1997, *SCORE’96 : Solar Convection and Oscillations and their Relationship*, 225, 241
- Parker, E. N. 1993, *ApJ*, 408, 707

Scherrer, P. H., et al. 1995, *Sol. Phys.*, 162, 129

Schou, J., et al. 1998, *ApJ*, 505, 390

Spiegel, E. A., & Zahn, J.-P., 1992 *A&A*, 265, 106

Thompson, M. J., et al. 1996, *Science*, 272, 1300

Zhao, J. 2007, *ApJ*, 664, L139

Zhao, J., Georgobiani, D., Kosovichev, A. G., Bensen, D., Stein, R. F., & Nordlund, Å. 2007, *ApJ*, 659, 848

Zhao, J., Kosovichev, A. G., & Duvall, T. L., Jr. 2001, *ApJ*, 557, 384

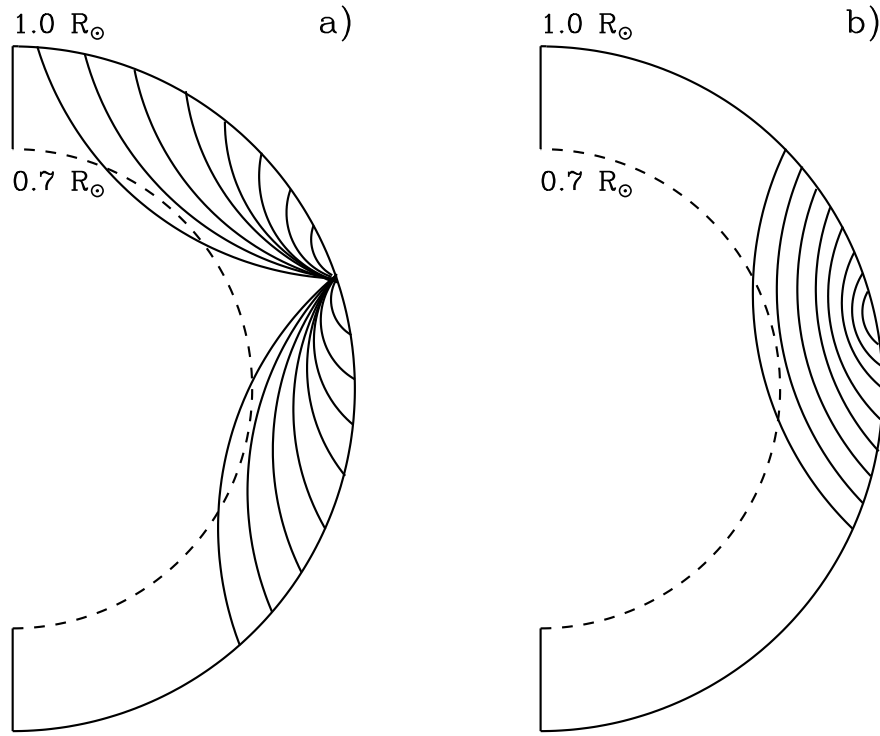


Fig. 1.— Sketches of wave paths in a meridional plane for two measurement schemes: a) surface-focusing and b) deep-focusing.

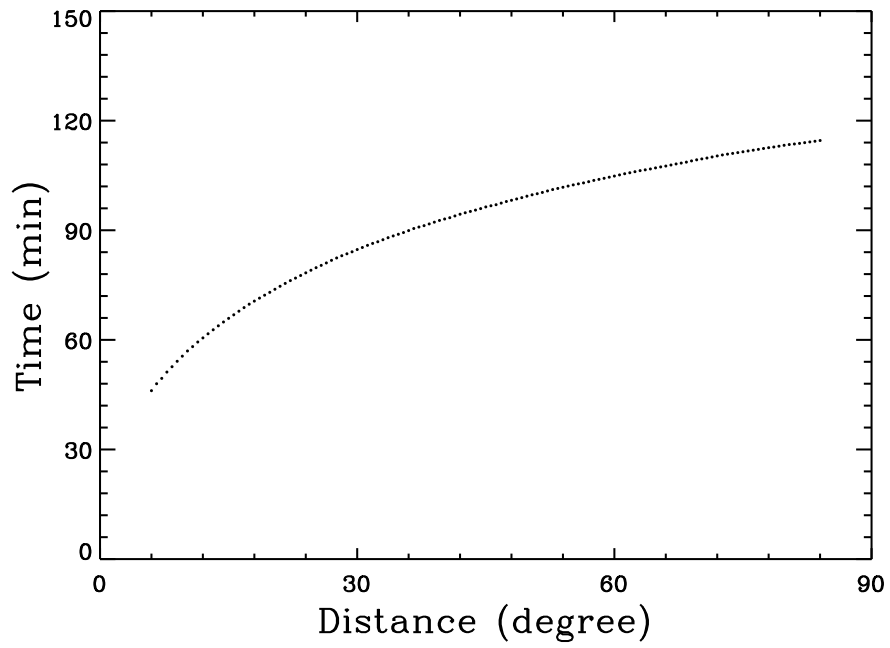


Fig. 2.— Acoustic phase travel time measured from the numerically simulated global wavefields using solar model S. The distance step is 0.6° in the heliographic coordinate.

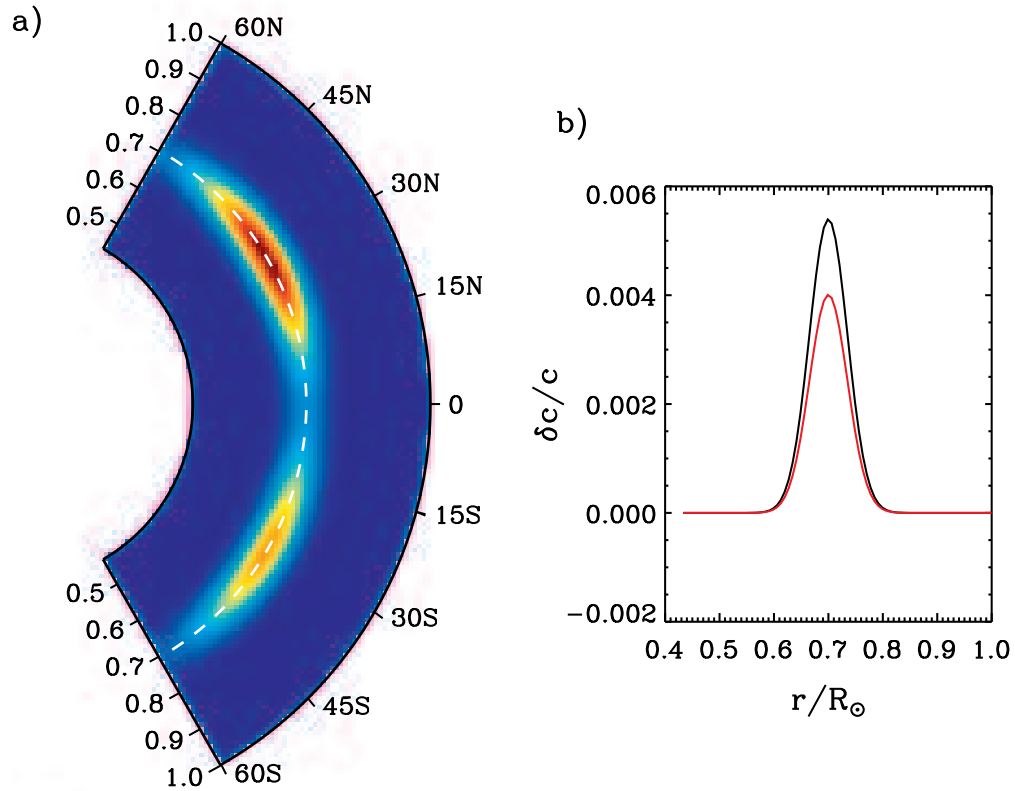


Fig. 3.— a) Sound-speed perturbation model in the tachocline region used in the numerical simulation of global acoustic wavefields. The perturbation maxima, 0.7% and 0.5%, are centered at $0.70R_{\odot}$ and latitude of 30° in Northern and Southern hemispheres, respectively. The white dashed curve indicates the radius of $0.70R_{\odot}$ (the bottom of the convection zone). b) Latitudinally averaged sound-speed perturbation of this tachocline model, with the black curve from the Northern hemisphere, and the red from the Southern.

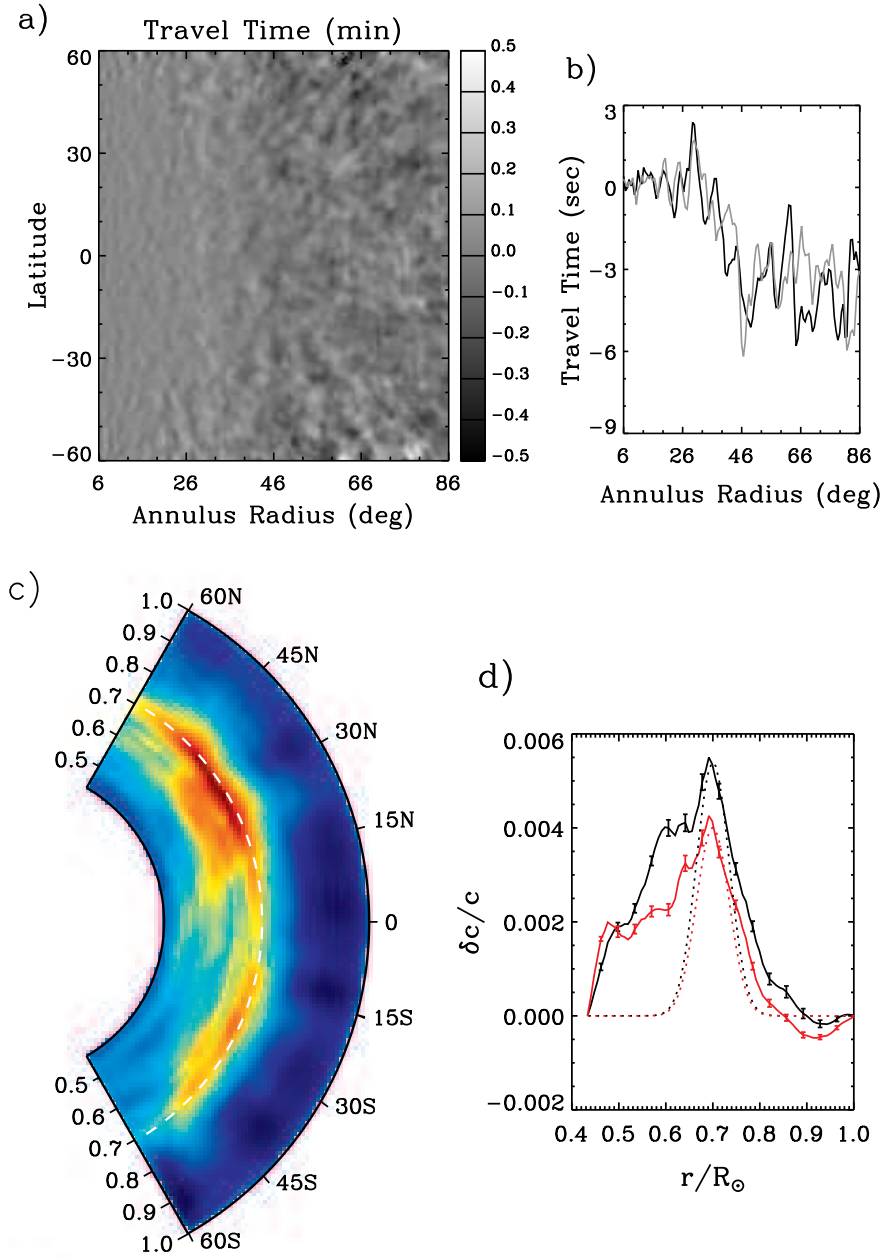


Fig. 4.— Measurements and inversion results for the surface-focusing measurement scheme: a) acoustic travel times measured from the numerical simulation with the tachocline model, relative to the travel times without tachocline; b) latitudinally averaged relative travel times, with dark from the Northern hemisphere and grey from the Southern; c) 2D inversion results for the sound-speed perturbation; d) latitudinally averaged inversion results, with solid lines showing inversions and dotted lines showing the averaged perturbation model. Dark lines are for the Northern hemisphere and the red lines are for the Southern. Errors bars indicate 2σ formal error estimates.

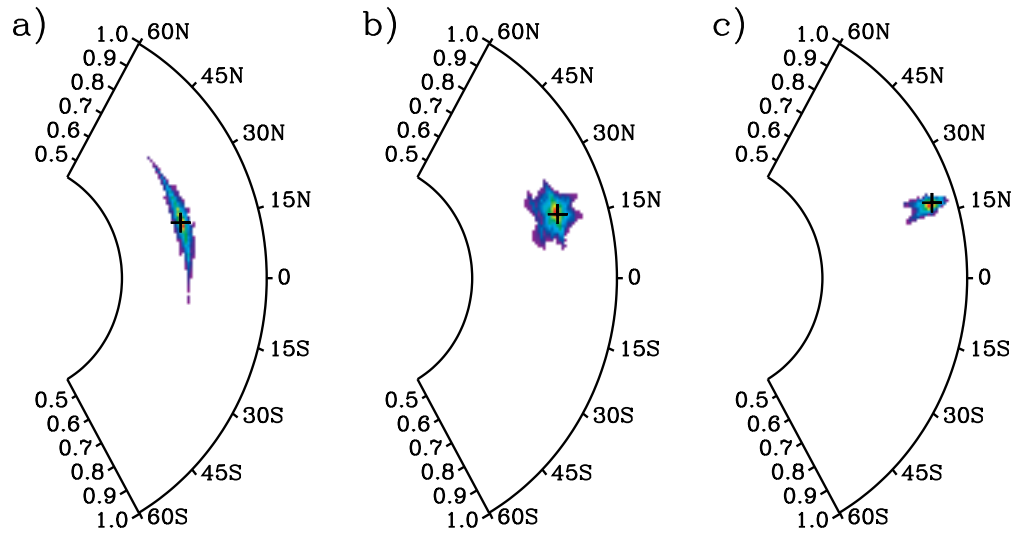


Fig. 5.— A sample of the averaging kernels for the surface-focusing inversions for the target locations at 18° latitude and a) $0.70R_{\odot}$, b) $0.80R_{\odot}$, and c) $0.90R_{\odot}$. The cross in each panel indicates the targeted location.

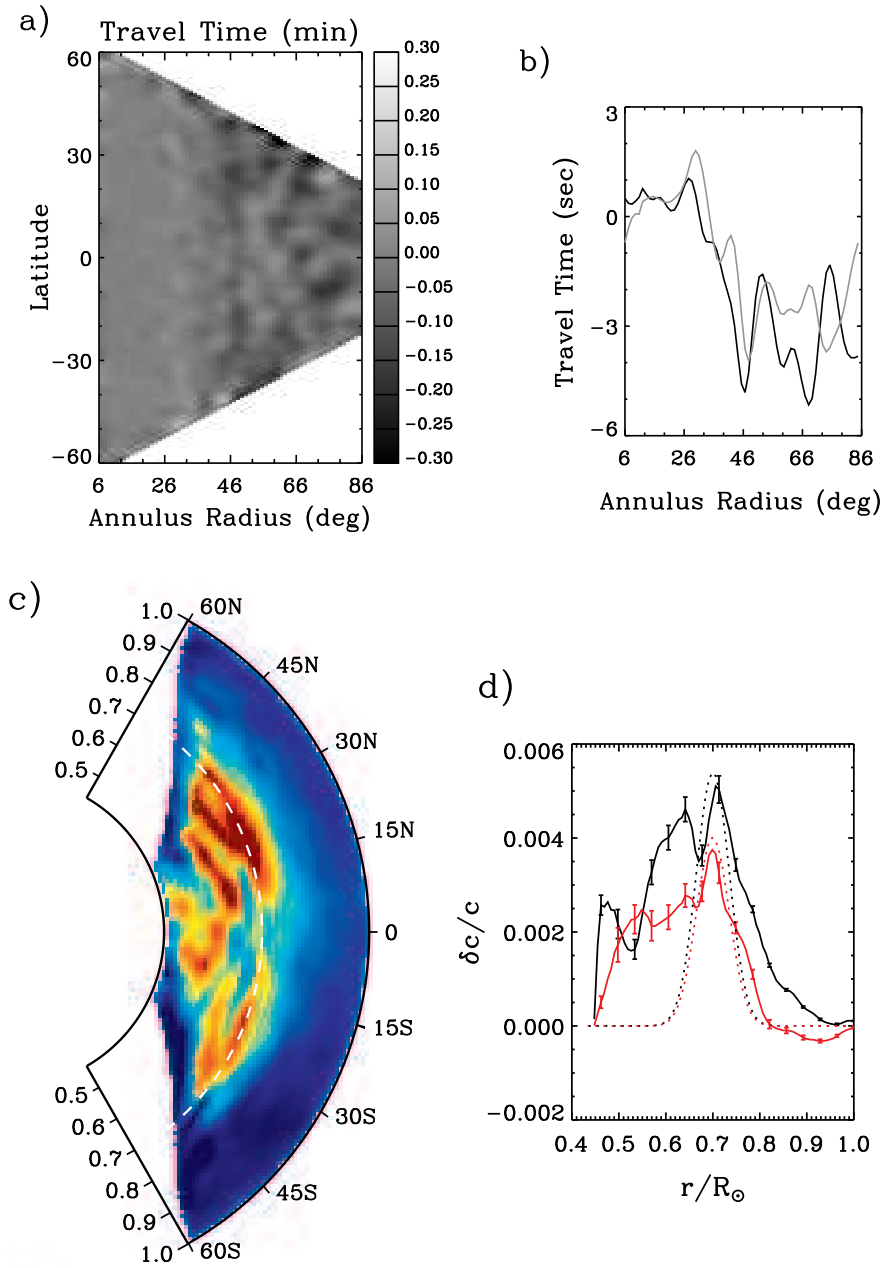


Fig. 6.— Same as Fig. 4, but for the deep-focusing scheme. Note that this scheme provides less coverage than the surface-focusing scheme.

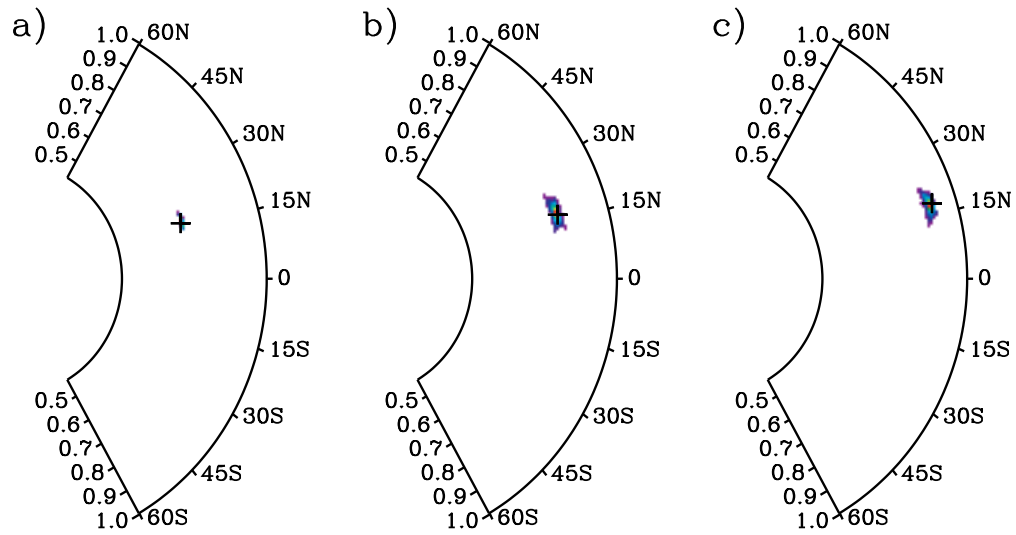


Fig. 7.— Same as Fig. 5, but for the deep-focusing scheme.

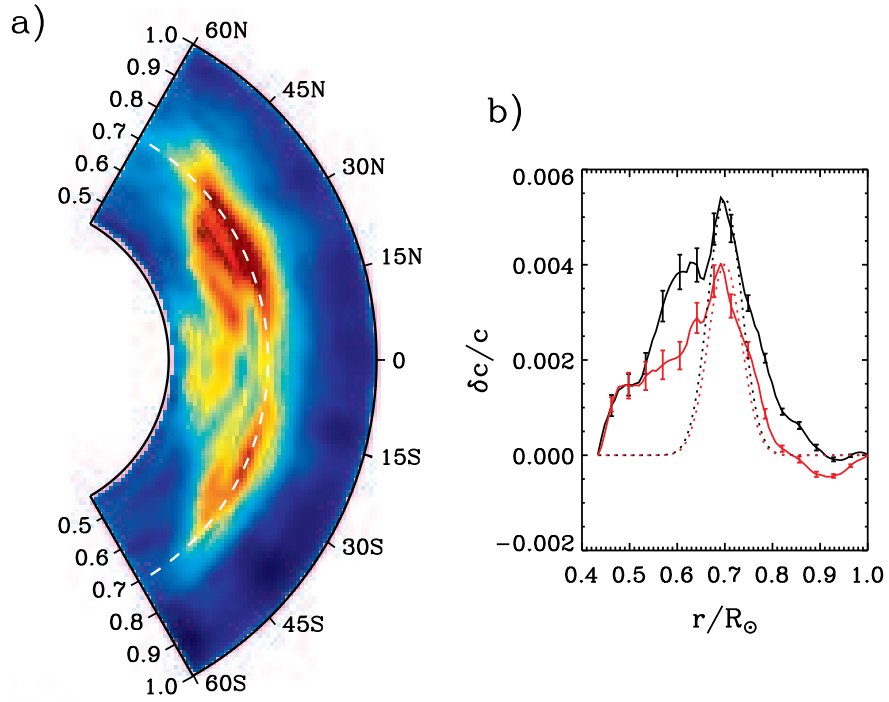


Fig. 8.— Same as panels c) and d) in Fig. 4, but for the combined inversion of the surface- and deep-focusing measurements.

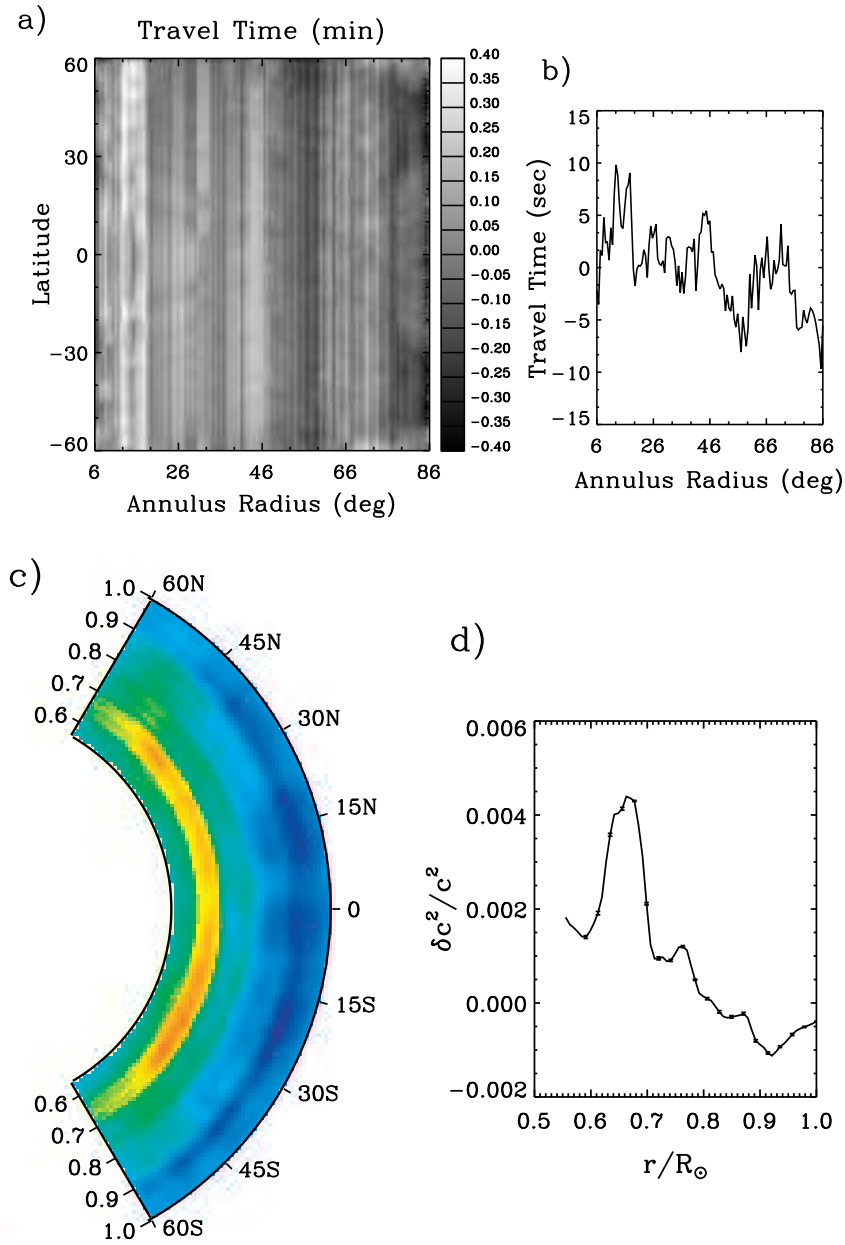


Fig. 9.— Same as Fig. 4, but for the SOHO/MDI medium- ℓ solar oscillation data and without showing separate hemispheric results.

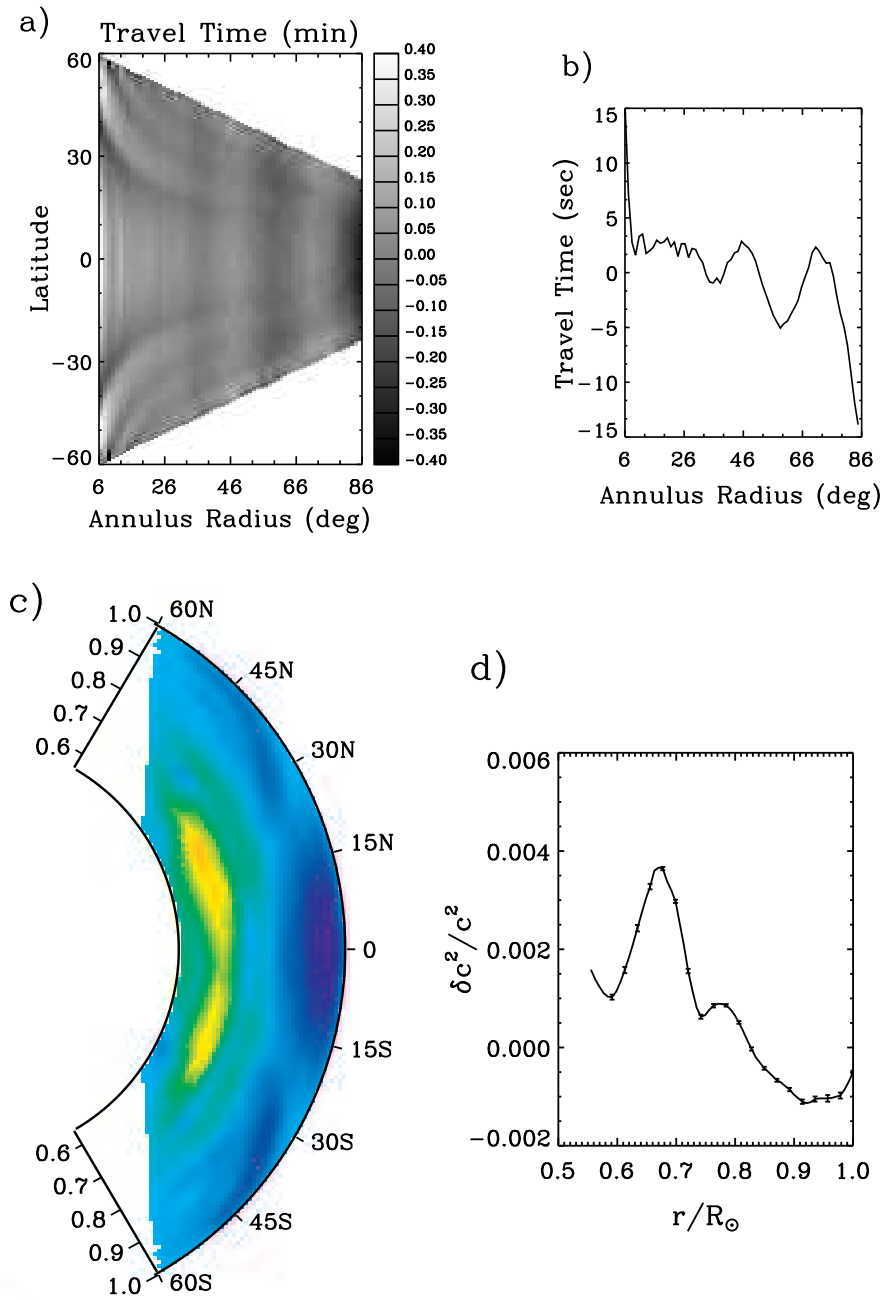


Fig. 10.— Same as Fig. 9, but for the deep-focusing scheme.

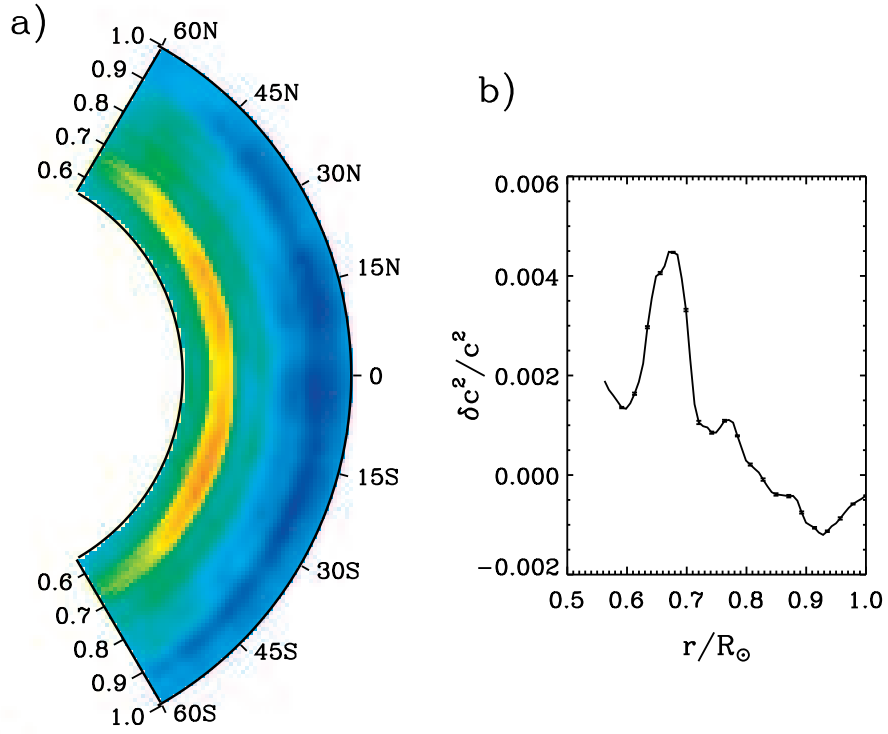


Fig. 11.— Same as panels c) and d) in Fig. 9, but for the combined inversion of the surface- and deep-focusing measurements.

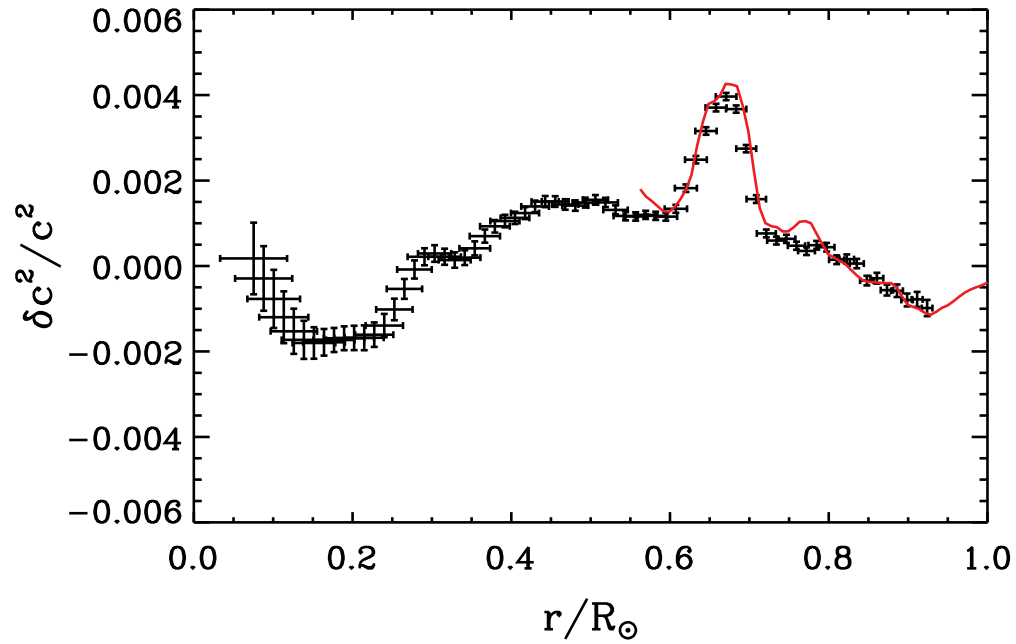


Fig. 12.— Comparison of the sound-speed perturbation obtained from global helioseismology (symbol with error bars; Kosovichev et al. 1997), and the inversion results obtained by combining surface- and deep-focusing measurements of acoustic travel times (solid curve).